Article

Alternative view of oxygen reduction on porous carbon electrocatalysts: the substance of complex oxygen-surface interactions

A — O_2 interacts with carbon surface features

B — cathodic current — Reduction takes place

C — cathodic current — Upon protonation OH^- are formed

D — cathodic current — Pore is available to adsorb another O_2

$2e^-$

Giacomo de Falco, Marc Florent, Jacek Jagiello, Yongqiang Cheng, Luke L. Daemen, Anibal J. Ramirez-Cuesta, Teresa J. Bandosz

tbandosz@ccny.cuny.edu

HIGHLIGHTS

Small pores, electron-rich surface, basic groups, and ethers enhance ORR on carbons

Ethers attract dissolved oxygen and increase accessibility of oxygen to pores

Strong adsorption potential in small hydrophobic pores attract O_2 from an electrolyte

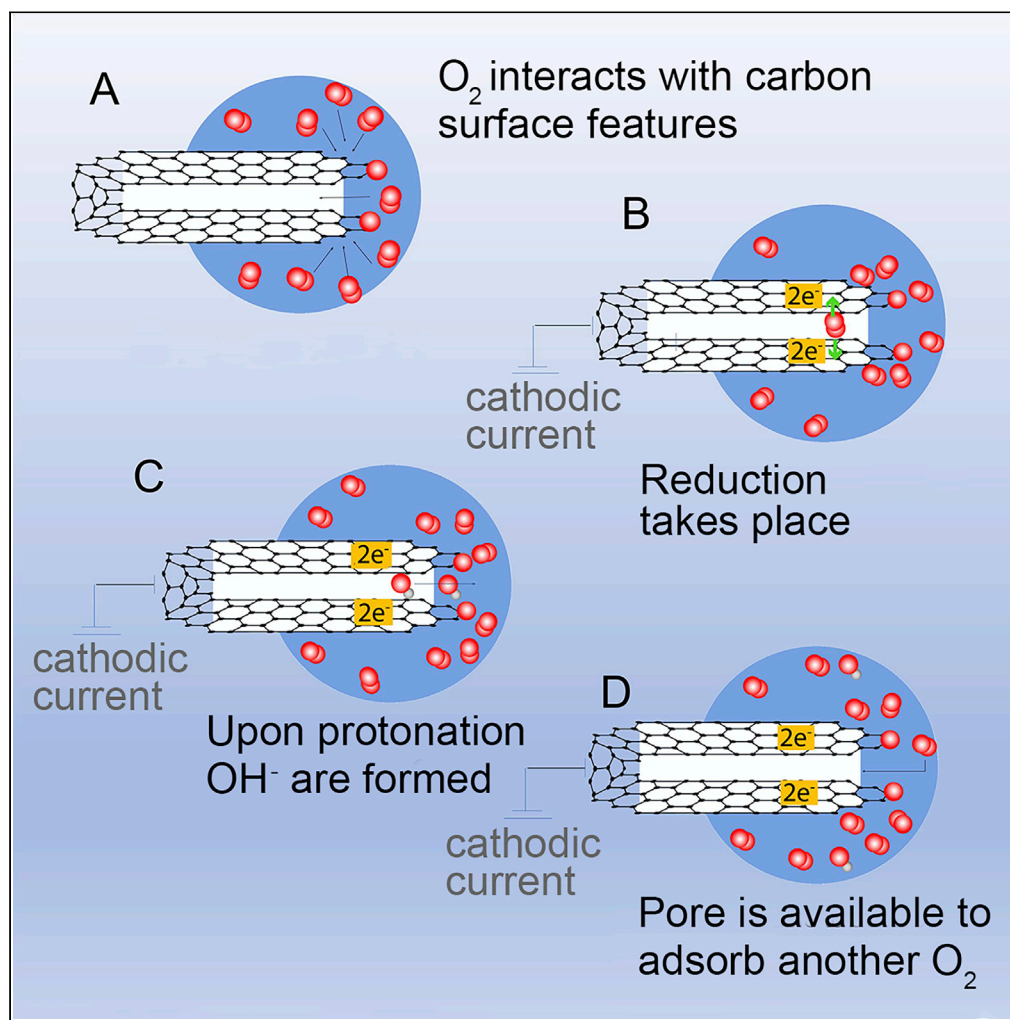Upon O_2 adsorption, O=O bonds break and O atoms accept electrons and H

Article

Alternative view of oxygen reduction on porous carbon electrocatalysts: the substance of complex oxygen-surface interactions

Giacomo de Falco,[1,4] Marc Florent,[1,4] Jacek Jagiello,[2] Yongqiang Cheng,[3] Luke L. Daemen,[3] Anibal J. Ramirez-Cuesta,[3] and Teresa J. Bandosz[1,*]

SUMMARY

Electrochemical oxygen reduction reaction (ORR) is an important energy-related process requiring alternative catalysts to expensive platinum-based ones. Although recently some advancements in carbon catalysts have been reported, there is still a lack of understanding which surface features might enhance their efficiency for ORR. Through a detailed study of oxygen adsorption on carbon molecular sieves and using inelastic neutron scattering, we demonstrated here that the extent of oxygen adsorption/interactions with surface is an important parameter affecting ORR. It was found that both the strength of O_2 physical adsorption in small pores and its specific interactions with surface ether functionalities in the proximity of pores positively influence the ORR efficiency. We have shown that ultramicropores and hydrophobic surface rich in ether-based groups and/or electrons enhance ORR on carbon electrocatalysts and the performance parameters are similar to those measured on Pt/C with the number of electron transfer equal to 4.

INTRODUCTION

Oxygen reduction reaction (ORR) is a strategically important energy-related application of carbon-based electrocatalysts (Chen et al., 2020; Liu and Dai, 2016; Ma et al., 2019; Shao et al., 2016; Tang and Zhang, 2017; Yan et al., 2018; Yang et al., 2013; Yu et al., 2011; Zhang et al., 2015). Even though the heteroatom-doped carbons (Chen et al., 2020; Choi et al., 2012; Ma et al., 2019; Shao et al., 2016; Tang and Zhang, 2017; Yan et al., 2018; Yu et al., 2011) gained the most attention owing to the specificity of N-, P-, S-, and B-based catalytic centers, some activity was also linked to the structural defects of disturbed graphene sheet edges (Greco et al., 2019; Jiang et al., 2015; Li et al., 2018; Xue et al., 2018), effects of oxygen groups (Zhang et al., 2018), porosity (Eisenberg et al., 2016; Ferrero et al., 2016; Gabe et al., 2019; Morais et al., 2019), or even pore sizes (Barrera et al., 2019a, 2019b; Encalada et al., 2017; Florent et al., 2019; Gabe et al., 2019; Seredych et al., 2016).

An explanation of the effect of porosity on the performance of electrocatalyst poses a challenge to traditional electrocatalysis concepts, and there are only few reports pointing out the role of this feature. One of the first reports addressing the possible effect of porosity on the efficiency of ORR was published by Tammeveski and coworkers (Kruusenberg et al., 2010). Then various articles on N-doped carbons suggested the importance of large transport pores/mesopores (Eisenberg et al., 2016; Ferrero et al., 2016; Mostazo-López et al., 2019; Quílez-Bermejo et al., 2017). Nevertheless, the first direct reports linking the effects of pore sizes to the ORR efficiency were published by our research group (Barrera et al., 2019a, 2019b; Encalada et al., 2017; Florent et al., 2019; Seredych et al., 2016). We have suggested that the reduction process might be driven by oxygen adsorption and that ultramicropores work as pseudocatalytic centers for ORR by promoting strong O_2 adsorption, which in turn helps with O=O bond splitting and thus promotes a 4 e− reduction path (Barrera et al., 2019b). Even though water can adsorb in carbon micropores, even hydrophobic, it was suggested that its adsorption occurs upon the formation of clusters with sizes of ∼0.5 nm (Iiyama et al., 2000). Those clusters are not expected to enter the smallest pores accessible to oxygen, and their heat of adsorption at a low surface coverage is smaller than that of oxygen (Park et al., 2019; Phillips et al., 1998; Salame and Bandosz, 2000). Moreover, this favorable energetics of oxygen adsorption might result in replacement of water by oxygen in ultramicropores. It has been also suggested that carbon with a

[1]Department of Chemistry and Biochemistry, The City College of New York, New York, NY 10031, USA

[2]Micromeritics Instrument Corporation, Norcross, GA 30093, USA

[3]Neutron Scattering Division, Oak Ridge National Laboratory, Oak Ridge, TN 37831, USA

[4]These authors contributed equally

*Correspondence: tbandosz@ccny.cuny.edu

https://doi.org/10.1016/j.isci.2021.102216

high surface area can show unusual ferromagnetism (Kaneko, 1996b) and oxygen, owing to its paramagnetic properties, can be strongly attracted to carbon on its surface. It can also exhibit strong spin-spin interactions (Kaneko, 1996a). Recently, the dependence of the ORR performance of carbons on the porosity has been also addressed by Ribeiro Pereira and coworkers (Morais et al., 2019), who found the dependence of the current density on the Brunauer–Emmett–Teller surface area. A direct effect of microporosity on the mechanism of ORR has been investigated by Cazorla-Amoros and co-workers (Gabe et al., 2019). Their mathematical model considered mass transfer rates, two reduction reactions, and different activity of ultra-micropores and supermicropores (narrow and wide micropores). The results suggested that the adsorption potentials and mass transfer between two types of pores are linked to the high activity of H_2O_2 reduction in narrow micropores.

Based on the above-addressed finding, and the need to refer to the observed phenomena/trends in more depth, in this article we evaluate very homogeneous porous carbon molecular sieves (CMS) as ORR catalysts, with an emphasis on their affinity to adsorb oxygen and/or interact with it. We hypothesize that adsorption of oxygen in small pores, both nonspecific and specific, contributes to the observed trends in the oxygen electroreduction efficiency. The engagement of inelastic neutron scattering (INS) technique permits us to investigate *in situ* changes in oxygen environment upon O_2 adsorption in carbon pores. To broaden the range of surface features, the CMS were oxidized to various degrees either in hot air or in nitric acid. Detailed analysis of their surfaces combined with O_2 adsorption and the ORR performance enables us to provide a direct proof of the effects of pore sizes and their affinity to attract oxygen via adsorption forces and that of surface hydrophobicity/chemistry on the efficiency of the ORR process. To the best of our knowledge, it is the first report attempting to link the ORR activity to the direct interactions of oxygen with porous carbons, both physical and chemical in nature.

RESULTS AND DISCUSSION

Porosity evaluation

Based on the shapes of the N_2 adsorption isotherms (Figure S1), the CS series of carbons are predominantly microporous. The pore size distributions (PSDs) (Figure 1) indicate the same sizes of small pores (0.57 and 1.27 nm) in both CMS; however, CS shows more homogeneity. CX has also a marked volume in pores between 4 and 40 nm, and its oxidation decreased the volume of micropores with a gradual appearance of mesopores. Air oxidation of CS did not affect its PSD, but for CS-Acid a dramatic change in PSD was found. The volume of pore smaller than 1 nm (ultramicropores) markedly decreased, which was accompanied by a decrease in size of supermicropores (1 nm < w < 2 nm). This indicates the collapse of the small pore walls due to the oxidative effect of acid on the carbon matrix.

The parameters of the pore structure calculated from N_2 adsorption isotherms are collected in Table 1. Because the calculated PSDs of most of our carbons show a minimum at about 1 nm, we have arbitrarily chosen this value as an upper size of ultramicropores. The surface area of CS is about 35% bigger than that of CX, and it is linked to its 38% higher volume of micropores, especially those between 1 and 2 nm. CS is predominantly microporous ($V_{mic}/V_t = 0.98$), whereas CX has a micro/meso nature ($V_{mic}/V_t = 0.49$). Acid oxidation of CS decreased its surface area by about 40% with almost 50% decrease in the micropore volume.

Electrocatalytic oxygen reduction

CV curves measured in O_2-saturated electrolytes (Figure S2) show well-pronounced oxygen reduction humps between 0.6 and 0.8 V versus RHE. Linear sweep voltammetry (LSV) curves measured in O_2-saturated electrolyte (Figures 2A and 2B) are typical for porous carbon catalysts with a sharp increase in current density below 0.8 V versus RHE. Two distinct ORR processes (Gabe et al., 2019) are clearly visible only for the CX series. CS-Air exhibits the highest current density of 3.4 mA cm^{-2}, and the lowest (2.5 mA cm^{-2}) is measured on CX and CX-Acid. For both series, oxidation increased the current density.

From a kinetic limiting current (Figure S3A) a kinetic current density (Figure 2C) was calculated using the geometrical surface areas of the electrodes. CS-Air and CX-Air have the highest current density at more negative potential (11 mA cm^{-2}), whereas at more positive potential CX outperforms CX-Air. The values measured on our CMSs are comparable to those reported in the literature on other carbon electrocatalysts (Chen et al., 2010; Eisenberg et al., 2016; Ferrero et al., 2016; Jorge et al., 2020; Qu et al., 2010). To account for the effect of S_{BET} and that of the electrochemically active surface area (36.81, 54.78, 21.03, 35.88, 57.81,
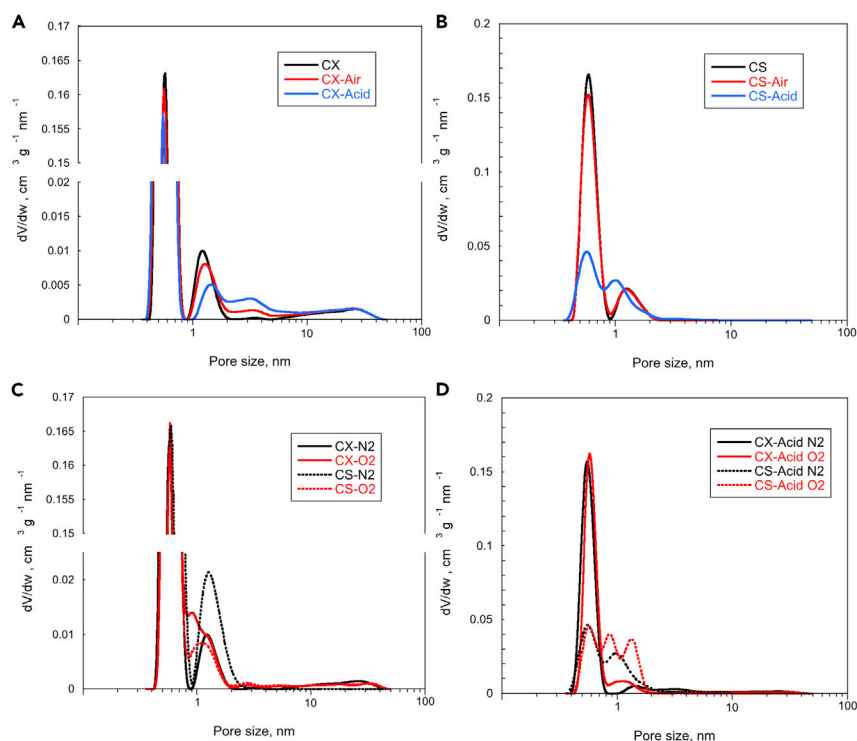
Figure 1. Porosity evaluation

(A) PSDs of CX series calculated from N_2 adsorption isotherms.

(B) PSDs of CS series calculated from N_2 adsorption isotherms.

(C) Comparison of PSDs calculated from N_2 and O_2 adsorption isotherms (denoted as N_2 and O_2, respectively) for the initial carbons.

(D) Comparison of PSDs calculated from N_2 and O_2 adsorption isotherms (denoted as N_2 and O_2, respectively) for the acid-oxidized carbons.

and 45.27 cm^2 for CX, CX-Air, CX-Acid, CS, CS-Air, and CS-Acid, respectively), the current density was normalized for these values (Figures S3B and S3C, respectively in the supplemental information). In these categories, the best performing samples are CS-Acid and CX-Acid, respectively.

In terms of the number of electron transfer and the amount of peroxide produced in the ORR process (Figures 2D and 2E, respectively) the best performing is CX on which n is very stable and almost 4 (3.98) (comparable to that on Pt/C [Florent et al., 2019]). The n values on other catalysts tested are also high (3.45–3.88), and they show the following decreasing trend: CS-Air > CS > CS-Acid > CX-Acid > CX-Air. The amount of peroxide produced is consistent with the number of electron transfer, and oxidized samples, with an exception of CS-Air, showed an increase in the % H_2O_2 formed.

Table 1. Comparison of the parameters of the pore structure calculated from N_2 and O_2 adsorption isotherms.

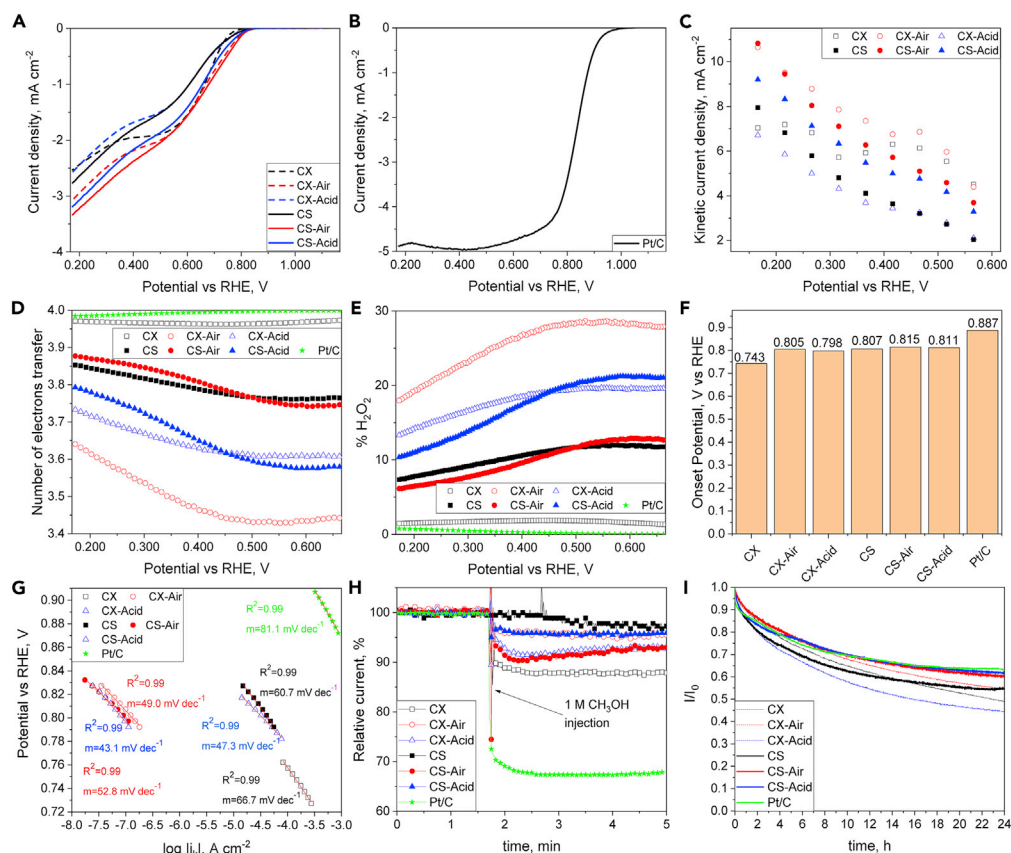| | S_{BET} $m^2\,g^{-1}$ | N_2 | | | | O_2 | | |
		S_{DFT} $m^2\,g^{-1}$	$V_{<1\ nm}$ $cm^3\,g^{-1}$	V_{mic} $cm^3\,g^{-1}$	V_t $cm^3\,g^{-1}$	$V_{<1\ nm}$ $cm^3\,g^{-1}$	V_{mic} $cm^3\,g^{-1}$	V_t $cm^3\,g^{-1}$
CX	920	1,133	0.300	0.350	0.715	0.309	0.361	0.678
CX-Air	915	1,157	0.297	0.346	0.738	0.302	0.353	0.684
CX-Acid	860	1,136	0.282	0.316	0.814	0.287	0.330	0.654
CS	1,210	1,348	0.351	0.485	0.496	0.357	0.500	0.516
CS-Air	1,195	1,195	0.346	0.491	0.505	0.351	0.507	0.530
CS-Acid	740	735	0.127	0.294	0.351	0.195	0.385	0.387

Figure 2. Electrocatalytic oxygen reduction
(A) LSV curves of all samples in O_2-saturated 0.1 M KOH at 2,000 rpm.
(B) LSV curve of Pt/C.
(C) Kinetic current density normalized per the geometrical surface area of the electrode.
(D) Number of electron transfer.
(E) Amount of peroxide formed.
(F) Onset potentials.
(G) Tafel plots.
(H) Tolerance to methanol.
(I) Stability of the catalysts.

The onset potential (Figure 2F) is the most positive on CS-Air (0.815 V versus RHE). Interestingly, on CX only 0.743 V versus RHE was measured. All other samples had similar onset potential values. As in the case of n, CX outstands other samples, but in this case in its low onset potential value.

Tafel plot slopes (Figure 2G) are in the range 43–66 mV dec^{-1}, and the best performing sample (the smallest slope) in this category is CS-Air and the worst one is CX. It is important to mention, the slopes measured on our catalysts are smaller than the slope for Pt/C indicating a fast kinetics of the electron transfer. All CMS catalysts are also better than Pt/C in terms of the tolerance to methanol crossover (Figure 2H), and when the stability (Figure 2I) is considered, CS-Acid and CS-Air show similar performance as Pt/C.

Surface chemistry analyses

The thermal analysis (TA) results (Figures 3A and 3B) show CX as very thermally stable carbon, whereas CS undergoes a significant weight loss (~13%) in a broad temperature range. That complex weight loss trend is linked to a broad range of oxygen functionalities such as quinone, ether, carbonyl, and phenol (Figueiredo et al., 1999). On the contrary, species present on the surface of CX are chemically homogeneous, and their high decomposition temperature suggests their ether nature (Petrescu et al., 2020). Oxidation of CS, especially with HNO_3, increased the population of surface oxygen groups, especially those decomposing
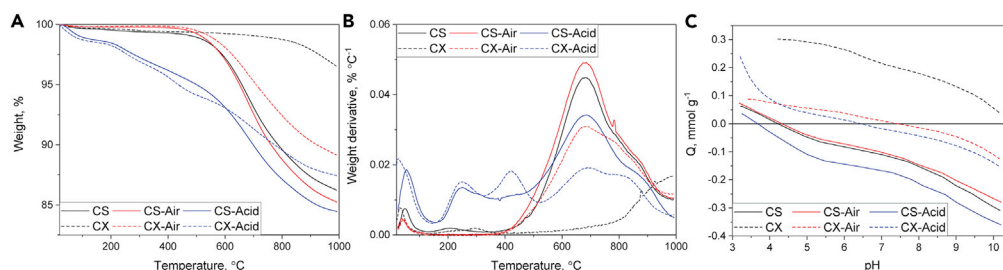
Figure 3. Surface chemistry analyses
(A) Thermogravimetric (TG) curves of the initial and oxidized samples.
(B) TG derivatives of the initial and oxidized samples.
(C) Proton-binding curves of the initial and oxidized samples

at a high temperature. On the other hand, carboxylic acids and lactones were introduced to CX-Acid (increase in weight loss at a low temperature [Bandosz and Ania, 2006; Figueiredo et al., 1999]). As a common feature, all samples show a weight loss at about 900°C, although of different extents.

Proton-binding curves and pH values (Figure 3C, Table 2) show CX as the only basic sample (proton consumption), and after oxidation some acidic groups were introduced (release of protons). On the other hand, oxidation of CS resulted in rather small changes in its acid-base properties. The pK_a distributions (Figures S4A and S4B) indicate that the CS series is more chemically heterogeneous than is the CX series. For the latter, acid oxidation increased the number of groups with $pK_a < 5.5$, associated with carboxylic acids (Jagiełło et al., 1994), and this is consistent with the trend in the thermal analysis results. The discrepancy with the TA data in terms of the extent of changes is only apparent because the thermally stable groups formed as a result of oxidation, as, for instance, quinones or ethers, do not exhibit an acid-base character in our pH experimental window. CX stands out among all other samples in its basic character, which, contrary to carbon acidity (Bandosz and Ania, 2006), is not well-defined, and many reports link it to Lewis sites associated with π electron-rich regions within the basal planes of graphitic microcrystals located away from the edges (Leon y Leon et al., 1992; Menéndez et al., 1997). The same number of dissociating groups on the surface of this carbon as that on CX-Air, in spite of a significant difference in their surface pH, suggests its electron-rich nature.

Interestingly, the X-ray photoelectron spectroscopy (XPS) results and their deconvolutions (Smith et al., 2016) (Table 3 and Figure S5) showed that oxidation of CMS did not change significantly the overall content of elements on the surface. Oxidation of CS with air affected the distribution of carbon-oxygen bonds very slightly. On the other hand, its oxidation with acid increased the contribution of C-O bonds, as estimated from both C 1s and O 1s spectra, and slightly decreased the overall oxygen content.

Identification of sites advancing ORR

As the potentiometric titration showed no marked changes in the numbers of dissociating groups, we linked the species containing C-O bonds to ethers (Nisola et al., 2020). CS-Acid is the only carbon sample that showed the higher contribution of C-O bonds than that of C=O. Thus, their presence might increase

Table 2. Surface pH and number of groups on the surface of the materials in mmol/g

Sample	pH	Strongly acidic 3 < pK_a < 5	Neutral 5 < pK_a < 8	Weakly acidic 8 < pK_a < 11	All
CS	4.8	0.17	0.08	0.21	0.46
CS-Air	4.6	0.19	0.09	0.18	0.46
CS-Acid	4.1	0.23	0.08	0.16	0.47
CX	8.1	0.02	0.10	0.25	0.37
CX-Air	5.7	0.04	0.07	0.20	0.31
CX-Acid	5.2	0.43	0.07	0.20	0.70

Table 3. Surface composition of CMS evaluated by XPS (in the % contribution). The atomic % of C and O on the surface is expressed in bold letters.

Binding energy eV	Bond assignment	CS	CS-Air	CS-Acid	CX	CX-Air	CX-Acid
C 1s		**84.5**	**87.2**	**88.6**	**88.4**	**91.0**	**89.2**
284.7–284.8	C–C sp^2	72.3	80.1	69.0	62.3	77.3	81.5
285.7–286.5	C–O (phenol, alcohol, ether, C-O-C)	15.4	11.2	17.9	26.8	11.6	9.9
287.2–287.5	C=O (carbonyl, quinone)	5.4	4.0	6.4	4.6	4.7	3.7
288.7–289.0	O=C–O (carboxyl)	4.4	3.2	4.5	6.1	4.0	3.0
289.5–290.5	π-π* satellite	2.5	1.5	2.2	0.1	2.4	1.9
O 1s		**15.5**	**12.8**	**11.4**	**11.6**	**9.0**	**10.8**
531.9–532.2	C=O	59.5	68.0	30.2	51.1	59.0	72.1
533–533.9	C–O, C-O-C	40.5	32.0	69.8	48.9	41.0	27.9

both the oxygen withdrawal from the electrolyte, its adsorption on the surface (via hydrophobicity), and its reduction to peroxide, which might be the first reduction step. As a result, CS-Acid shows relatively good overall performance in ORR in spite of its smallest volume of ultramicropores that we consider as the main factor governing the ORR reduction on microporous carbons. Moreover, the oxygen-containing groups, either ethers or those of acid-base properties, exist rather in larger pores and/or are incorporated to the edges of pore walls, and the very small surface area of CS and its relatively small degree of microporosity suggest the high density of ethers on its surface. They have hydrophobic character and thus attract oxygen (Ensing et al., 2019; Menger and Chlebowski, 2005), and by continuously providing that oxygen to pores, where reduction occurs, they might contribute to the continuous increase in the current, as measured by LSV.

On the other hand, the CX is very active owing to its basic/electron-rich surface, which adds to the efficiency of the cathodic reduction. Moreover, its surface also contains ethers (a high contribution of C-O bonds) and is hydrophobic (lack of acidic group). The deconvolution of O 1s core energy level of CX-Acid clearly shows the majority of oxygen in the C=O configurations (Figure S5), which is consistent with the presence of carboxylic acids contributing to the acidic character of its surface. This marked decrease in the population of electrons on the surface as a result of oxidation led to a decrease in the ORR efficiency in terms of *n*.

Linking ORR to interaction of oxygen with the CMS surface

The interpretation of ORR on our CMS is not very straightforward. We hypothesize that the availability of small pores for oxygen along with its nonspecific and specific interactions with the carbon surface plays an important role in the reduction process. The results discussed above suggest that ethers affect/increase O_2 adsorption not only by providing hydrophobicity (Ensing et al., 2019; Menger and Chlebowski, 2005). However, the predominant feature of CMS is a high volume of ultramicropores, and it should govern both the penetration of surface by electrolyte with dissolved oxygen and adsorption of that oxygen. As N_2 and O_2 molecules are similar when measured in equilibrium (Salame and Bandosz, 2000), and therefore the porous structure seen by them should be similar (Jagiello and Kenvin, 2019), the comparison of the extent of oxygen adsorption on the surface, especially in the small pores, with that of nitrogen might help us to better understand the behavior of CMS as the ORR catalyst. Here we need to clarify that even though CMS were tested and used for O_2/N_2 separation, which might falsely suggest differences in their pore accessibility, those approaches are usually based on the difference in the kinetics of the adsorption (Andrade et al., 2020; Nabais et al., 2006). The adsorption of N_2 and O_2 on CMS was studied in detail by Bae and Lee (2005), and it was found that even though the amounts adsorbed of both molecules at equilibrium on CMS were very similar, the kinetics markedly differed, and O_2, owing to its paramagnetic properties (Kaneko, 1996b), exhibited a much higher sorption rate than did N_2. In the approach used here the adsorption equilibrium is reached and all fluid-surface parameters have been taken into consideration to calculate PSDs (Jagiello and Kenvin, 2019).

PSDs calculated from O_2 adsorption isotherms using non-local density functional theory (NLDFT) (Jagiello and Kenvin, 2019) (see Figures S6–S8) are compared in Figures 1C and 1D with those calculated from N_2
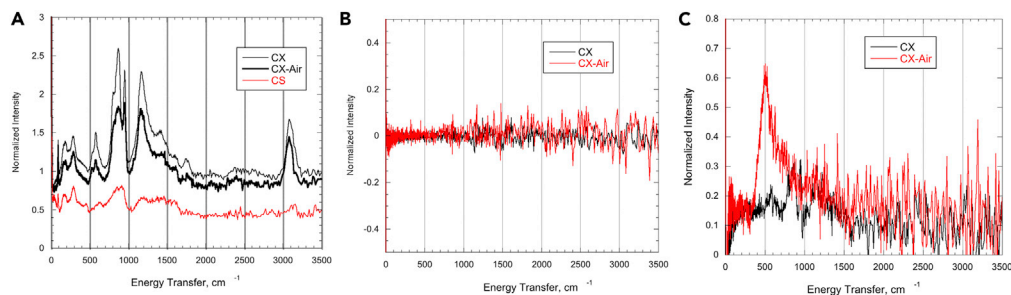
Figure 4. Inelastic neutron scattering

(A) The comparison of INS spectra for blank CX, CX-Air, and CS.

(B) Difference between the INS spectra exposed to oxygen and blank for CX and CX-Air.

(C) Difference between the INS spectra of the samples exposed to water and oxygen and those exposed to water before oxygen exposure, for CX and CX-Air.

adsorption isotherms. The volumes of the specific pore sizes, $V_{<1\,nm}$, V_{mic}, and V_t, calculated either from N_2 or O_2 adsorption isotherms are summarized in Table 1. The sizes of ultramicropores detected by O_2 and N_2 are similar for CS and CX. The differences are visible for larger micropores, $> \sim 1$ nm, where consistently oxygen shows slightly smaller pores of higher heterogeneity, especially for CX and CS-Acid, than does nitrogen. As the combined surface chemistry analyses (Ania et al., 2020) suggest the marked contribution of ethers on the surface of these CMS, this pattern might reflect an oxygen engagement, in specific interactions with those groups. For all CMS but CS-Acid the amount of oxygen adsorbed in micropores (presented as a pore volume, V_{mic}) is slightly (2%–4%) greater than that of N_2. It might be related to its paramagnetic properties and affinity to carbons surface, whereas nitrogen is known to form dimers (Bae and Lee, 2005; Kaneko, 1996a, 1996b). Interestingly, the total amount of oxygen adsorbed on CX is smaller than that of N_2, especially for CX-Acid where 20% less oxygen is adsorbed than nitrogen. A reason for this might be in different electronic properties of CX than those of CS that affect the ferromagnetism of a carbon surface and thus interactions of oxygen with carbon atoms and also in spin-spin interactions between oxygen molecules (Kaneko, 1996a, 1996b). Therefore, the marked number of acidic groups of this carbon might hinder accessibility of the electrolyte with dissolved oxygen to the hydrophobic carbon surface, and this effect combined with a decrease in the pore volume might decrease the ORR activity of this carbon. For the CS series the amount of oxygen adsorbed on the surface is between 5% and 10% higher than that of N_2, which suggests the contribution of specific interactions. In CS-Acid the volumes of ultramicropores and micropores seen by O_2 are 50% and 30% higher, respectively, than those detected by N_2. This supports our hypothesis that oxygen groups of these carbons, and particularly ethers, by attracting oxygen enhance the withdrawal from the electrolyte advance oxygen reduction.

To further investigate the O_2-carbon surface environment, inelastic neutron scattering (INS) spectra were measured on selected CMS, exposed to oxygen, and exposed to water with dissolved oxygen. As blank measurements CX and CX-Air and CS spectra in vacuum (Figure 4A) show mainly C-H bonds (Li et al., 2017) (e.g., C-H stretching at 3,100 cm^{-1}, C-H bending near 1,000 cm^{-1}) and the high intensity of the CX spectrum confirms its electron-rich nature.

The change of the spectra due to oxygen exposure of CX and CX-Air is negligible (within error/uncertainty) (Figure 4B), indicating the lack of any redox reaction and hydrogen transfer in the absence of water. On the other hand, the exposure to both water and oxygen altered the spectra (Figure S9) and on CX-Air much more water was adsorbed than on CX. The negligible amount of water retained on the surface of CX is a direct support of its hydrophobicity. This water on CX-Air is present as both bulk ice (the sharp edge between 500 and 600 cm^{-1} in Figure S9) and in a less confined form (the broad band between 400 and 1,000 cm^{-1}) (Hood et al., 2020). The differences in INS spectra (between $H_2O + O_2$ and H_2O exposure) (Figure 4C) show new OH species formed on CX-Air as a result of oxygen reduction, as indicated by the peak between 400 and 1,000 cm^{-1}. This peak cannot be due to H_2O for the lack of the translational peaks below 300 cm^{-1} (Hood et al., 2020). No apparent evidence of the OH formation on CX (the small features around 1,000 cm^{-1} are due to a minor mis-subtraction of the background spectrum, see Figure S9), which is not surprising as the sample is very hydrophobic and absorbed a negligible amount of water at our experimental conditions with a rather short equilibration time used.
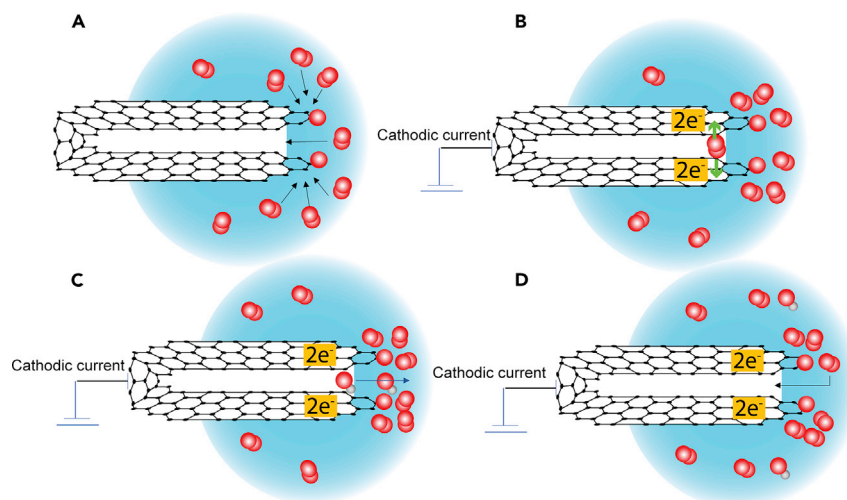
Figure 5. Visualization of ORR on CMS

(A) Withdrawal of oxygen from an electrolyte by the hydrophobic surface of small pores and their high adsorption potential; attraction of oxygen to ethers.

(B) Splitting of O_2 molecule due to strong adsorption forces from both pore walls followed by its reduction.

(C) With the help of cathodic current the reduction of oxygen in pores takes place accompanied by its protonation owing to the proximity of water; OH^- is formed and released to water owing to its affinity to the water phase.

(D) Oxygen accumulated on ethers enters pores to be further reduced.

As a summary of our findings, Figure 5 presents the processes advancing the efficiency of ORR on CMS of distinct microporosity and of hydrophobic surface linked to the very small pore sizes, electron-rich carbon surface, and presence of ethers.

In conclusion, we have shown that the specific types of interactions of oxygen with carbon electrocatalyst surfaces are the factors strongly affecting the efficiency of the ORR process. For this study we have chosen CMS of a very defined pore structure and of surface chemistry governed only by the various engagement of oxygen groups (no other heteroatoms). Although the ultramicroporosity was the predominant structural feature, the carbons differed in surface acid-base properties and in the population of ethers. The results indicated that besides the porosity, the electron-rich surface (basic) and engagement of oxygen in surface ethers enhanced ORR. The electron-rich carbon matrix, by providing abundance of electrons apparently advanced the cathodic reduction process. Ethers attracted oxygen and concentrated it at the pore entrances, enhancing the efficiency of the further electron transfer in the pores with adsorbed oxygen. Both the electron-rich surface and ethers provided hydrophobicity of pores needed to withdraw molecular oxygen from the electrolyte, which, upon its adsorption in small pores, underwent the bond splitting and the efficient four-electron transfer. This process involves also simultaneous protonation, and even though oxygen is isolated from water in the pores due to the strong adsorption potential, this water as a proton source is in very close proximity, at the pore entrance. Adsorption of molecular oxygen showed the sensitivity of the carbon surface to O_2 with either ethers and/or electron providing/governing the specific interactions. INS results supported our hypothesis that the reduction of oxygen and its protonation on the carbon surface takes place, even without an applied potential. This process can be only further enhanced when electroreduction in the presence of an electrolyte is involved. Therefore, the results of this research show new directions to modify carbon surface toward an increased efficiency of ORR. They might markedly contribute to ongoing efforts on replacing noble metal-based catalysts in energy-related applications. We would like to emphasize that the objective of our work was presenting an alternative view of the ORR on porous carbons and not the best performing metal-free catalysts.

Limitations of the study

The carbons studied do not exhibit an exceptionally high performance as ORR electrocatalysts, although they are on par with some other metal-free electrocatalysts reported in the literature. They were chosen owing to their relatively homogeneous pore structure and small pore sizes with an intention to support our hypothesis on the role of small pores as ORR pseudocatalytic centers. Even though the complex

process discussed in this study involves ethers, carbon surface hydrophobicity, basicity, and physical adsorption, our analysis should be considered as simplified because other sites on carbons, including defects, must also affect the ORR. The results discussed are limited to ORR in basic electrolytes.

Resource availability

Lead contact

Further information and requests for resources and reagents should be directed to and will be fulfilled by the lead contact, Teresa J. Bandosz PhD, DSc (tbandosz@ccny.cuny.edu).

Materials availability

This study did not generate new unique reagents.

Data and code availability

This study did not generate any code. The data supporting the current study are available from the corresponding author on request.

METHODS

All methods can be found in the accompanying transparent methods supplemental file.

SUPPLEMENTAL INFORMATION

Supplemental information can be found online at https://doi.org/10.1016/j.isci.2021.102216.

AUTHOR CONTRIBUTIONS

G.d.F., experimental planning, electrochemical measurements, data analysis, manuscript writing and editing, visualization, revision; M.F., experimental planning, surface chemistry characterization, data analyses, manuscript writing and editing, visualization, revision; J.J.,measurements of N_2 and O_2 adsorption, data analysis, manuscript editing, visualization; Y.C., neutron scattering data collection and analysis, manuscript editing; L.L.D., neutron scattering data collection and analysis; A.J.R.-C., neutron scattering data collection and analysis; T.J.B., resources, experimental planning, data analysis, visualization, manuscript writing and editing, revision.

DECLARATION OF INTERESTS

The authors declare no competing interests.

REFERENCES

Andrade, M., Rodrigues, S.C., and Mendes, A. (2020). High performing CMS adsorbent for O_2/ N_2 separation. Microporous Mesoporous Mater. *296*, 109989.

Ania, C.O., Armstrong, P.A., Bandosz, T.J., Beguin, F., Carvalho, A.P., Celzard, A., Frackowiak, E., Gilarranz, M.A., László, K., Matos, J., et al. (2020). Engaging nanoporous carbons in "beyond adsorption" applications:

characterization, challenges and performance. Carbon *164*, 69–84.

Bae, Y.S., and Lee, C.H. (2005). Sorption kinetics of eight gases on a carbon molecular sieve at elevated pressure. Carbon *43*, 95–107.

Bandosz, T.J., and Ania, C.O. (2006). Chapter 4. Surface chemistry of activated carbons and its

characterization, Interface Science and Technology. In Activated Carbon Surfaces in Environmental Remediation, T.J. Bandosz, ed. (Elsevier), pp. 159–229.

Barrera, D., Florent, M., Kulko, M., and Bandosz, T.J. (2019a). Ultramicropore-influenced mechanism of oxygen electroreduction on metal-free carbon catalysts. J. Mater. Chem. A *7*, 27110–27123.

Barrera, D., Florent, M., Sapag, K., and Bandosz, T.J. (2019b). Insight into the mechanism of oxygen reduction reaction on micro/mesoporous carbons: ultramicropores versus nitrogen-containing catalytic centers in ordered pore structure. ACS Appl. Energy Mater. 2, 7412–7424.

Chen, L., Xu, X., Yang, W., and Jia, J. (2020). Recent advances in carbon-based electrocatalysts for oxygen reduction reaction. Chin Chem. Lett. 31, 626–634.

Chen, Z., Higgins, D., and Chen, Z. (2010). Nitrogen doped carbon nanotubes and their impact on the oxygen reduction reaction in fuel cells. Carbon 48, 3057–3065.

Choi, C.H., Park, S.H., and Woo, S.I. (2012). Binary and ternary doping of nitrogen, boron, and phosphorus into carbon for enhancing electrochemical oxygen reduction activity. ACS Nano 6, 7084–7091.

Eisenberg, D., Prinsen, P., Geels, N.J., Stroek, W., Yan, N., Hua, B., Luo, J.-L., and Rothenberg, G. (2016). The evolution of hierarchical porosity in self-templated nitrogen-doped carbons and its effect on oxygen reduction electrocatalysis. RSC Adv. 6, 80398–80407.

Encalada, J., Savaram, K., Travlou, N.A., Li, W., Li, Q., Delgado-Sánchez, C., Fierro, V., Celzard, A., He, H., and Bandosz, T.J. (2017). Combined effect of porosity and surface chemistry on the electrochemical reduction of oxygen on cellular vitreous carbon foam catalyst. ACS Catal. 7, 7466–7478.

Ensing, B., Tiwari, A., Tros, M., Hunger, J., Domingos, S.R., Pérez, C., Smits, G., Bonn, M., Bonn, D., and Woutersen, S. (2019). On the origin of the extremely different solubilities of polyethers in water. Nat. Commun. 10, 2893.

Ferrero, G.A., Preuss, K., Fuertes, A.B., Sevilla, M., and Titirici, M.M. (2016). The influence of pore size distribution on the oxygen reduction reaction performance in nitrogen doped carbon microspheres. J. Mater. Chem. A 4, 2581–2589.

Figueiredo, J.L., Pereira, M.F.R., Freitas, M.M.A., and Órfão, J.J.M. (1999). Modification of the surface chemistry of activated carbons. Carbon 37, 1379–1389.

Florent, M., Wallace, R., and Bandosz, T.J. (2019). Oxygen electroreduction on nanoporous carbons: textural features vs nitrogen and boron catalytic centers. ChemCatChem 11, 851–860.

Gabe, A., Ruiz-Rosas, R., González-Gaitán, C., Morallón, E., and Cazorla-Amorós, D. (2019). Modeling of oxygen reduction reaction in porous carbon materials in alkaline medium. Effect of microporosity. J. Power Sources 412, 451–464.

Greco, C., Cosentino, U., Pitea, D., Moro, G., Santangelo, S., Patanè, S., D'Arienzo, M., Fiore, M., Morazzoni, F., and Ruffo, R. (2019). Role of the carbon defects in the catalytic oxygen reduction by graphite nanoparticles: a spectromagnetic, electrochemical and computational integrated approach. Phys. Chem. Chem. Phys. 21, 6021–6032.

Hood, Z.D., Cheng, Y., Evans, S.F., Adhikari, S.P., and Parans Paranthaman, M. (2020). Unraveling

the structural properties and dynamics of sulfonated solid acid carbon catalysts with neutron vibrational spectroscopy. Catal. Today 358, 387–393.

Iiyama, T., Ruike, M., and Kaneko, K. (2000). Structural mechanism of water adsorption in hydrophobic micropores from in situ small angle X-ray scattering. Chem. Phys. Lett. 331, 359–364.

Jagiełło, J., Bandosz, T.J., and Schwarz, J.A. (1994). Carbon surface characterization in terms of its acidity constant distribution. Carbon 32, 1026–1028.

Jagiello, J., and Kenvin, J. (2019). Consistency of carbon nanopore characteristics derived from adsorption of simple gases and 2D-NLDFT models. Advantages of using adsorption isotherms of oxygen (O_2) at 77K. J. Colloid Interface Sci 542, 151–158.

Jiang, Y., Yang, L., Sun, T., Zhao, J., Lyu, Z., Zhuo, O., Wang, X., Wu, Q., Ma, J., and Hu, Z. (2015). Significant contribution of Intrinsic carbon defects to oxygen reduction activity. ACS Catal. 5, 6707–6712.

Jorge, A.B., Jervis, R., Periasamy, A.P., Qiao, M., Feng, J., Tran, L.N., and Titirici, M.-M. (2020). 3D carbon materials for efficient oxygen and hydrogen electrocatalysis. Adv. Energy Mater. 10, 1902494.

Kaneko, K. (1996a). Chapter 2.10 Micropore filling mechanism in inorganic sorbents. In Stud Surf Sci Catal, A. Dąbrowski and V.A. Tertykh, eds. (Elsevier), pp. 573–598.

Kaneko, K. (1996b). Molecular assembly formation in a solid nanospace. Colloids Surf. A 109, 319–333.

Kruusenberg, I., Leis, J., Aruulepp, M., and Tammeveski, K. (2010). Oxygen reduction on carbon nanomaterial-modified glassy carbon electrodes in alkaline solution. J. Solid State Electrochem. 14, 1269–1277.

Leon y Leon, C.A., Solar, J.M., Calemma, V., and Radovic, L.R. (1992). Evidence for the protonation of basal plane sites on carbon. Carbon 30, 797–811.

Li, D., Jia, Y., Chang, G., Chen, J., Liu, H., Wang, J., Hu, Y., Xia, Y., Yang, D., and Yao, X. (2018). A defect-driven metal-free electrocatalyst for oxygen reduction in acidic electrolyte. Chem 4, 2345–2356.

Li, Y., Cheng, Y., Daemen, L.L., Veith, G.M., Levine, A.M., Lee, R.J., Mahurin, S.M., Dai, S., Naskar, A.K., and Paranthaman, M.P. (2017). Neutron vibrational spectroscopic studies of novel tire-derived carbon materials. Phys. Chem. Chem. Phys. 19, 22256–22262.

Liu, X., and Dai, L. (2016). Carbon-based metal-free catalysts. Nat. Rev. Mater. 1, 16064.

Ma, R., Lin, G., Zhou, Y., Liu, Q., Zhang, T., Shan, G., Yang, M., and Wang, J. (2019). A review of oxygen reduction mechanisms for metal-free carbon-based electrocatalysts. NPJ Comput. Mater. 5, 78.

Menéndez, J.A., Xia, B., Phillips, J., and Radovic, L.R. (1997). On the modification and characterization of chemical surface properties of

activated carbon: microcalorimetric, electrochemical, and thermal desorption probes. Langmuir 13, 3414–3421.

Menger, F.M., and Chlebowski, M.E. (2005). Is the ether group hydrophilic or hydrophobic? Langmuir 21, 2689–2695.

Morais, R.G., Rey-Raap, N., Figueiredo, J.L., and Pereira, M.F.R. (2019). Glucose-derived carbon materials with tailored properties as electrocatalysts for the oxygen reduction reaction. Beilstein J. Nanotechnol. 10, 1089–1102.

Mostazo-López, M.J., Salinas-Torres, D., Ruiz-Rosas, R., Morallón, E., and Cazorla-Amorós, D. (2019). Nitrogen-doped Superporous activated carbons as electrocatalysts for the oxygen reduction reaction. Materials (Basel) 12, 1346.

Nabais, J.M.V., Carrott, P.J.M., Carrott, M.M.L.R., Padre-Eterno, A.M., Menéndez, J.A., Dominguez, A., and Ortiz, A.L. (2006). New acrylic monolithic carbon molecular sieves for O_2/N_2 and CO_2/CH_4 separations. Carbon 44, 1158–1165.

Nisola, G.M., Parohinog, K.J., Cho, M.K., Burnea, F.K.B., Lee, J.Y., Seo, J.G., Lee, S.-P., and Chung, W.-J. (2020). Covalently decorated crown ethers on magnetic graphene oxides as bi-functional adsorbents with tailorable ion recognition properties for selective metal ion capture in water. Chem. Eng. J. 389, 123421.

Park, D., Ju, Y., Kim, J.-H., Ahn, H., and Lee, C.-H. (2019). Equilibrium and kinetics of nitrous oxide, oxygen and nitrogen adsorption on activated carbon and carbon molecular sieve. Sep. Purif. Technol. 223, 63–80.

Petrescu, S., Avramescu, S., Musuc, A.M., Neatu, F., Florea, M., and Ionita, P. (2020). Crown-ether functionalized graphene oxide for metal ions sequestration. Mater. Res. Bull. 122, 110643.

Phillips, J., Xia, B., and Menéndez, J.A. (1998). Calorimetric study of oxygen adsorption on activated carbon. Thermochim. Acta 312, 87–93.

Qu, L., Liu, Y., Baek, J.-B., and Dai, L. (2010). Nitrogen-doped graphene as efficient metal-free electrocatalyst for oxygen reduction in fuel cells. ACS Nano 4, 1321–1326.

Quílez-Bermejo, J., González-Gaitán, C., Morallón, E., and Cazorla-Amorós, D. (2017). Effect of carbonization conditions of polyaniline on its catalytic activity towards ORR. Some insights about the nature of the active sites. Carbon 119, 62–71.

Salame, I.I., and Bandosz, T.J. (2000). Adsorption of water and methanol on micro- and mesoporous wood-based activated carbons. Langmuir 16, 5435–5440.

Seredych, M., Szczurek, A., Fierro, V., Celzard, A., and Bandosz, T.J. (2016). Electrochemical reduction of oxygen on hydrophobic ultramicroporous PolyHIPE carbon. ACS Catal. 6, 5618–5628.

Shao, M., Chang, Q., Dodelet, J.-P., and Chenitz, R. (2016). Recent advances in electrocatalysts for oxygen reduction reaction. Chem. Rev. 116, 3594–3657.

CellPress
OPEN ACCESS

Smith, M., Scudiero, L., Espinal, J., McEwen, J.-S., and Garcia-Perez, M. (2016). Improving the deconvolution and interpretation of XPS spectra from chars by ab initio calculations. Carbon *110*, 155–171.

Tang, C., and Zhang, Q. (2017). Nanocarbon for oxygen reduction electrocatalysis: dopants, edges, and defects. Adv. Mater. *29*, 1604103.

Xue, L., Li, Y., Liu, X., Liu, Q., Shang, J., Duan, H., Dai, L., and Shui, J. (2018). Zigzag carbon as efficient and stable oxygen reduction

electrocatalyst for proton exchange membrane fuel cells. Nat. Commun. *9*, 3819.

Yan, X., Jia, Y., and Yao, X. (2018). Defects on carbons for electrocatalytic oxygen reduction. Chem. Soc. Rev. *47*, 7628–7658.

Yang, Z., Nie, H., Chen, X.a., Chen, X., and Huang, S. (2013). Recent progress in doped carbon nanomaterials as effective cathode catalysts for fuel cell oxygen reduction reaction. J. Power Sources *236*, 238–249.

Yu, L., Pan, X., Cao, X., Hu, P., and Bao, X. (2011). Oxygen reduction reaction mechanism on

nitrogen-doped graphene: a density functional theory study. J. Catal. *282*, 183–190.

Zhang, H., Lv, K., Fang, B., Forster, M.C., Dervişoğlu, R., Andreas, L.B., Zhang, K., and Chen, S. (2018). Crucial role for oxygen functional groups in the oxygen reduction reaction electrocatalytic activity of nitrogen-doped carbons. Electrochim. Acta *292*, 942–950.

Zhang, J., Xia, Z., and Dai, L. (2015). Carbon-based electrocatalysts for advanced energy conversion and storage. Sci. Adv. *1*, e1500564.

Supplemental information

Alternative view of oxygen reduction

on porous carbon electrocatalysts: the substance

of complex oxygen-surface interactions

Giacomo de Falco, Marc Florent, Jacek Jagiello, Yongqiang Cheng, Luke L. Daemen, Anibal J. Ramirez-Cuesta, and Teresa J. Bandosz

SUPPLEMENTAL INFORMATION

Transparent Methods

Materials: Polymer-based Carbosieve S-II and Carboxen 572 CMSs were obtained from Millipore and used as received or oxidized. They are referred to as CS and CX, respectively. CS and CX were oxidized by heating them for 3 h at 350 $^{\circ}$C in air, and the carbons obtained in this process are referred to by adding the suffix –Air. To impose more pronounced changes in surface chemistry, CS and CX were stirred in concentrated nitric acid at 80 $^{\circ}$C for 45 minutes. Then, the resulting samples were filtered and washed in a Soxhlet apparatus until a constant pH. The samples were dried at 60°C in air. The oxidized materials were referred to as CS-Acid and CX-Acid.

Surface characterization: Adsorption isotherms of N_2 and O_2 were measured at -197 $^{\circ}$C using the high-resolution Micromeritics 3Flex instrument equipped with a high-vacuum system, three micropore ports, and three 0.1 Torr pressure transducers. The samples were degassed under vacuum at 120 $^{\circ}$C overnight prior to the adsorption measurements. The pore size distribution (PSD) calculations are performed using molecular models based on the two-dimensional version of the nonlocal density functional theory (2D-NLDFT) (Jagiello and Olivier, 2013). The 2D-NLDFT models take into account the surface heterogeneity and roughness of the carbon surface. It was demonstrated (Jagiello and Kenvin, 2019; Jagiello and Olivier, 2013) that the PSD results derived using these models are free from typical artifacts observed when the standard one-dimensional NLDFT models were used (Jagiello and Olivier, 2013; Ustinov et al., 2006). In addition to N_2 data, O_2 isotherms are used for the PSD calculations. The advantage of using O_2 is in its smaller quadrupole moment compared to nitrogen (Jagiello and Kenvin, 2019; Jagiello et al., 2020).

Thermogravimetric analysis (TGA) was carried out with an SDT Q600 (TA instruments) thermal analyzer by heating the samples up to 1000 °C at a rate of 10 °C/min in an Argon flow (100 mL/min).

The potentiometric titration measurements were performed using an 888 Titrando automatic titrator (Metrohm). Suspensions of the sample in $NaNO_3$ (0.1M) were titrated with NaOH (0.1 M) starting from pH ~ 3.2 (HCl 0.1M was added to adjust the pH if necessary) up to pH ~ 10. The proton binding curve, Q, was derived from the titration data and pK_a distribution $f(pK_a)$ (Jagiełło et al., 1994) was obtained using a SAIEUS procedure (Jagiello, 1994). The experimental titration/pH measurement error is 2% for the surface pH measurement and about 10% for the total number of surface group assuming that the same mass of carbon was used for the analysis.

The XPS analysis was performed on a 200 μm diameter analysis area with a Physical Electronics PHI 5000 VersaProbe II spectrometer using an Al Kα X-ray radiation (50 W, 15 kV, 1486.6 eV) source with a take-off angle of 45° and a pass energy of 29.35 eV.

Inelastic neutron scattering (INS): INS experiments were performed at the VISION beamline, Spallation Neutron Source, Oak Ridge National Laboratory. About the same amount (1.5g) of each sample (CX, CX-Air, and CS) was loaded in an aluminum sample holder. The samples were first degassed under vacuum at 120 ^{o}C, and then measured at -268 ^{o}C to collect the INS spectra. The samples were then exposed to 2 bars of pure oxygen at room temperature for two hours, after which they were cooled back to -268 ^{o}C again to collect INS spectra. The samples were further degassed under vacuum at 120 ^{o}C, and then 350 μL of water was added. After equilibrating at 100 ^{o}C, the samples were then measured at -268 ^{o}C for INS spectra. The hydrated samples were exposed to oxygen again under the same conditions, before the final INS measurement at -268 ^{o}C.

Electrochemical oxygen reduction reaction (ORR): The electrochemical analyses were conducted with a computer-controlled WaveDriver 40 bipotentiostat (Pine Research Instrumentation). 5 mg of the carbon powder was dispersed in 1 ml of ethanol and 0.5 ml of 1 wt.% of a Nafion solution and sonicated for at least 60 minutes to obtain a catalyst ink. A three-electrode system was used

for electrochemical tests. A rotating glassy carbon electrode with a gold ring was used as a working electrode. The glassy carbon was loaded with 10 µL of the catalyst ink. The surface area of the electrode was equal to 0.196 cm^2 and typically 0.03 mg of carbon were deposited on the electrode. A reference electrode was Ag/AgCl (all results are recalculated to RHE for easy comparison), and a counter electrode - a graphite rod. The three electrodes were immersed in 60 ml of a 0.1 M KOH electrolyte for overnight before the beginning of the experiment.

Cyclic voltammograms (CV) were measured in N_2/O_2 at 100 (only in the case of N_2) and 5 mV s^{-1} on the disk. Linear scan voltammetry (LSV) tests were performed from 1.17 to 0.18 V vs RHE between 400 to 2000 rpm. A ring potential was set at 1.07 V vs RHE. From the LSV data, the number of electron transfer (*n*) and percentage of peroxide generated were calculated from equations 1 and 2, respectively.

$$n = \frac{4I_d}{I_d + \frac{I_d}{N}} \qquad (1)$$

$$\%H_2O_2 = \frac{200\frac{I_r}{N}}{I_d + \frac{I_r}{N}} \qquad (2)$$

In the equations above, I_d and I_r are the disk and ring currents measured with RRDE, respectively.

Kinetic current curves were derived using the Koutecky-Levich equation:

$$\frac{1}{I_d} = \frac{1}{I_k} + \frac{1}{I_l} = \frac{1}{Bw^{1/2}} + \frac{1}{I_k} \qquad (3)$$

where I_k is a kinetic current and I_l is a diffusion limited current.

The electrochemically active surface area (ECSA) was calculated from a double layer capacitance, measured by recording CV's in the non-faradaic region at various scan rates, (5 to 750 mV s^{-1}).

A double layer capacitance C_{DL} was obtained from equation 4:

$$C_{DL} = \frac{i_c + i_a}{2v} \qquad (4)$$

where i_a and i_c are the anodic and cathodic currents, respectively.

ECSA were derived from C_{DL}, using equation 5:

$$ECSA = \frac{C_{DL}}{C_S} \qquad (5)$$

where C_S is the specific capacitance of carbon black and it equals to 27.5 $\mu F\ cm^{-2}$.

The stability of the catalyst was investigated analyzing the trend of the current at the potential (set at the maximum of the ORR reduction hump) with a constant O_2 flow through the electrolyte. Methanol tolerance experiments were conducted by adding 2.5 mL of methanol into the 60 ml of electrolyte solution (methanol concentration in the electrolyte solution ~1M). The onset potential was calculated by using the SODDM method (de Falco et al., 2020). The Tafel slope was evaluated by plotting the potential as a function of $log(|j_k|)$ where j_k is a kinetic current density obtaining by the following equation:

$$j_k = \frac{j\ j_l}{j_k - j} \qquad (6)$$

j_k is the kinetic current density obtained by correcting the LSV current density, j, for the diffusion limiting current density j_l (Nunes et al., 2015). The Tafel plot was calculated in the most active region of the potential (near the onset potential region) (Guidelli et al., 2014).

References

de Falco, G., Florent, M., De Rosa, A., and Bandosz, T.J. (2020). Proposing an unbiased oxygen reduction reaction onset potential determination by using a Savitzky-Golay differentiation procedure. J Colloid Interface Sci.

Guidelli, R., Compton, R.G., Feliu, J.M., Gileadi, E., Lipkowski, J., Schmickler, W., and Trasatti, S. (2014). Defining the transfer coefficient in electrochemistry: An assessment (IUPAC Technical Report). Pure Appl Chem *86*, 245-258.

Jagiello, J. (1994). Stable Numerical Solution of the Adsorption Integral Equation Using Splines. Langmuir *10*, 2778-2785.

Jagiełło, J., Bandosz, T.J., and Schwarz, J.A. (1994). Carbon surface characterization in terms of its acidity constant distribution. Carbon *32*, 1026-1028.

Jagiello, J., and Kenvin, J. (2019). Consistency of carbon nanopore characteristics derived from adsorption of simple gases and 2D-NLDFT models. Advantages of using adsorption isotherms of oxygen (O_2) at 77 K. J Colloid Interface Sci *542*, 151-158.

Jagiello, J., Kenvin, J., Ania, C.O., Parra, J.B., Celzard, A., and Fierro, V. (2020). Exploiting the adsorption of simple gases O_2 and H_2 with minimal quadrupole moments for the dual gas characterization of nanoporous carbons using 2D-NLDFT models. Carbon *160*, 164-175.

Jagiello, J., and Olivier, J.P. (2013). 2D-NLDFT adsorption models for carbon slit-shaped pores with surface energetical heterogeneity and geometrical corrugation. Carbon *55*, 70-80.

Nunes, M., Rocha, I.M., Fernandes, D.M., Mestre, A.S., Moura, C.N., Carvalho, A.P., Pereira, M.F.R., and Freire, C. (2015). Sucrose-derived activated carbons: electron transfer properties and application as oxygen reduction electrocatalysts. RSC Adv *5*, 102919-102931.

Ustinov, E.A., Do, D.D., and Fenelonov, V.B. (2006). Pore size distribution analysis of activated carbons: Application of density functional theory using nongraphitized carbon black as a reference system. Carbon *44*, 653-663.
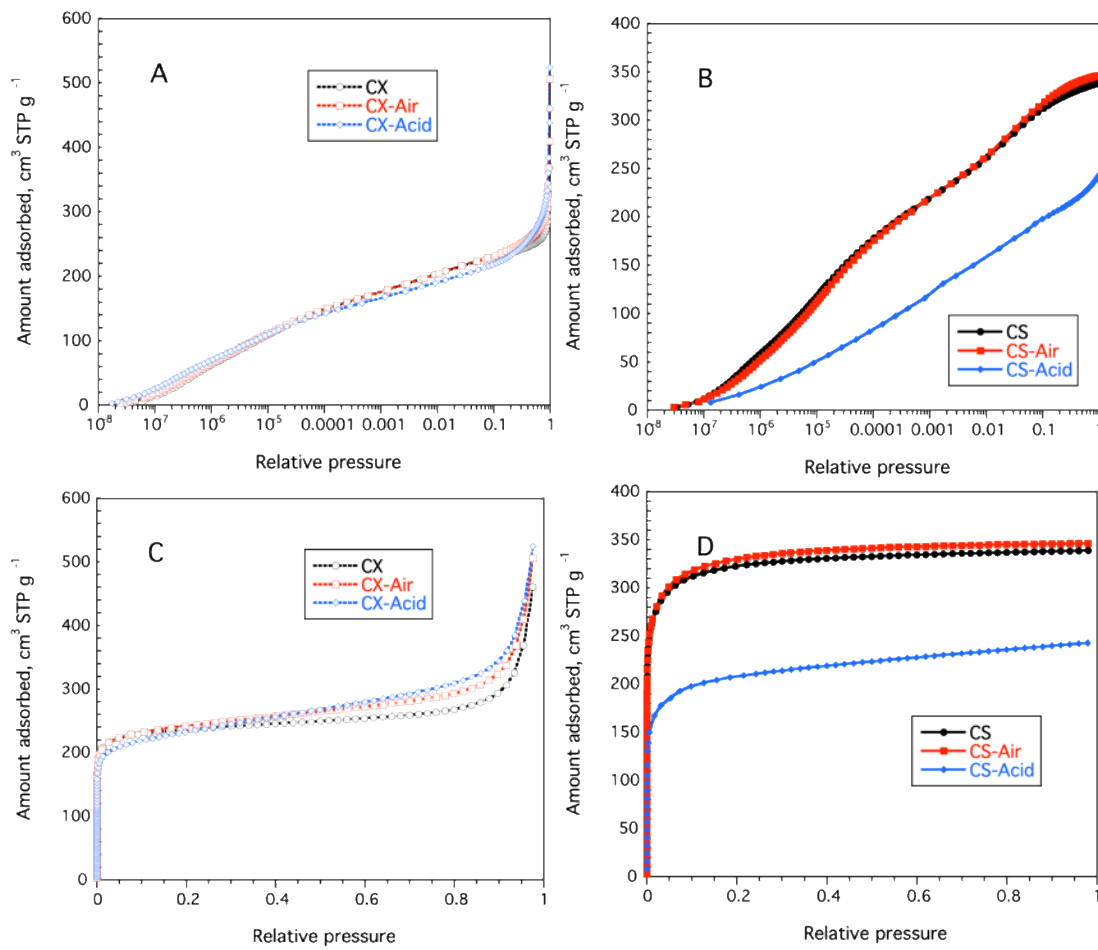
Supplemental Figures

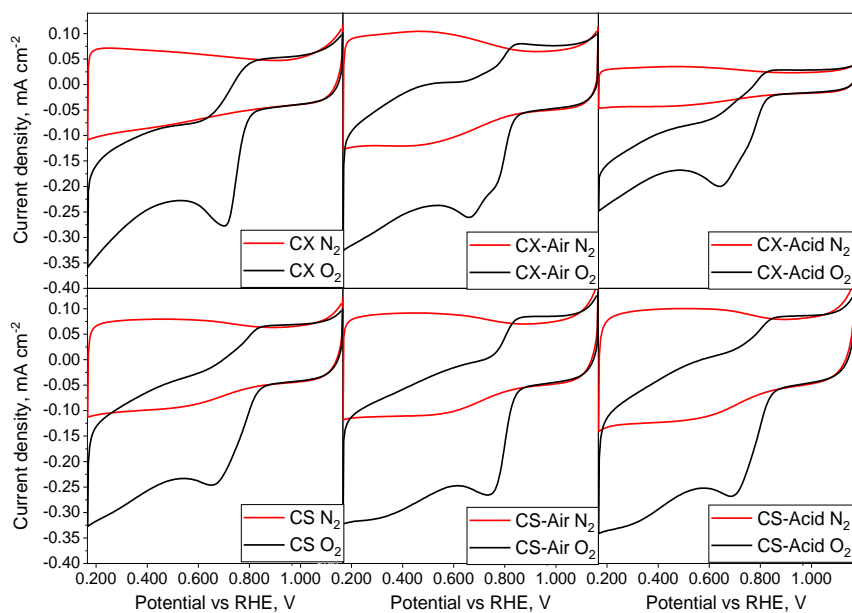Figure 1S. **Measured nitrogen adsorption isotherms** (Related to Fig.1).

Figure 2S. **CV curves of all the investigated samples measured in 0.1 M KOH saturated with N₂ and O₂** (related to Fig.2).
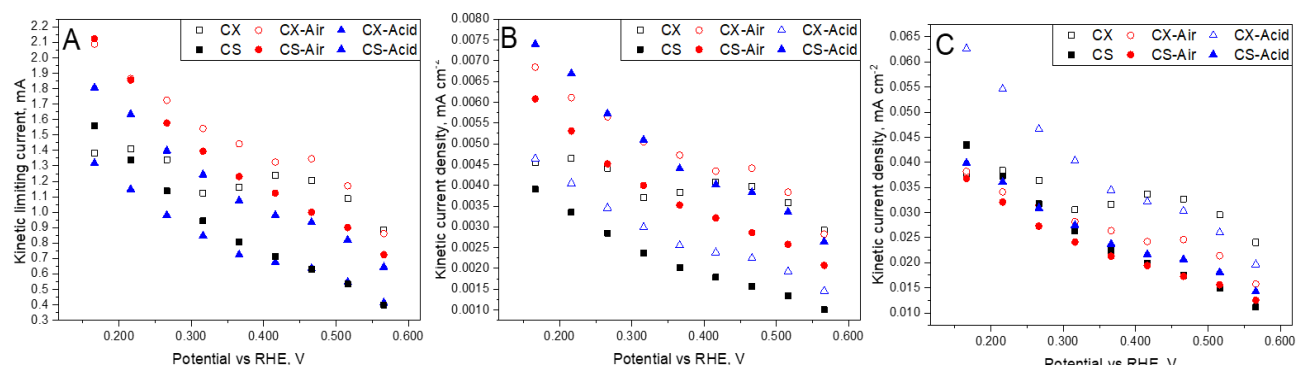

Figure 3S. **Kinetic current** (related to Fig.2)
A) kinetic limiting current
B) kinetic current density normalized by S_{BET}
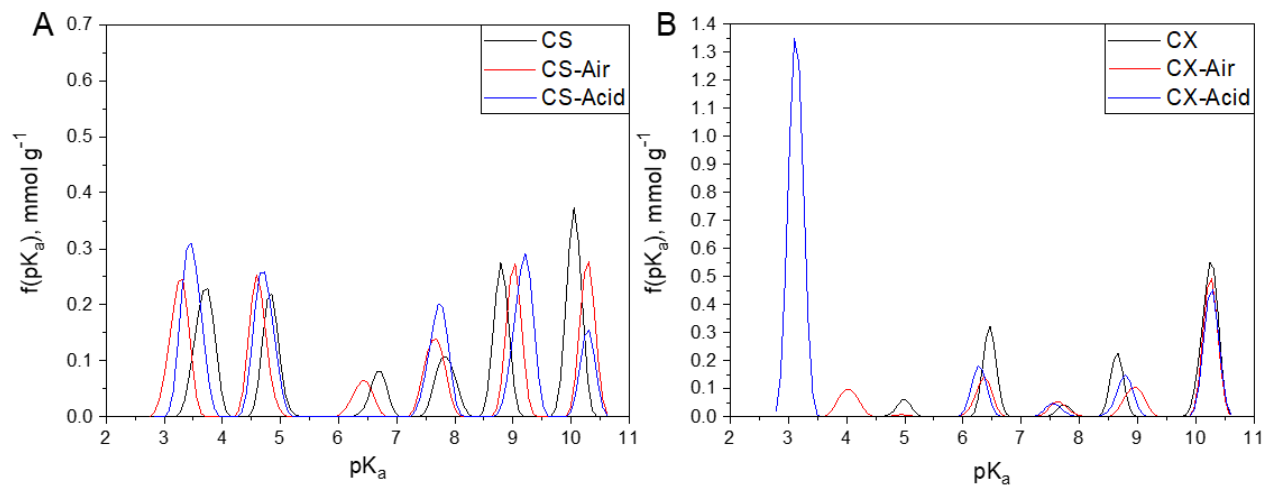C) kinetic current density normalized by ECSA

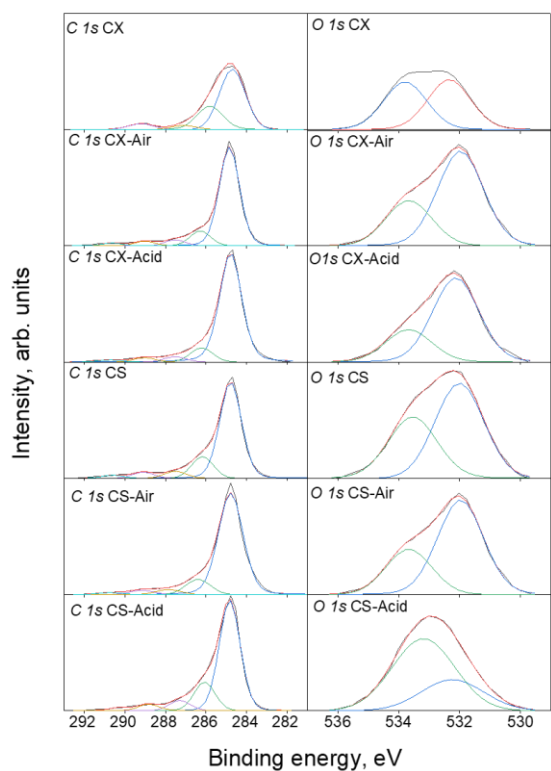Figure 4S. **pK$_a$ distributions** (related to Fig 3 and Table 2).
A)CS series
B)CX series

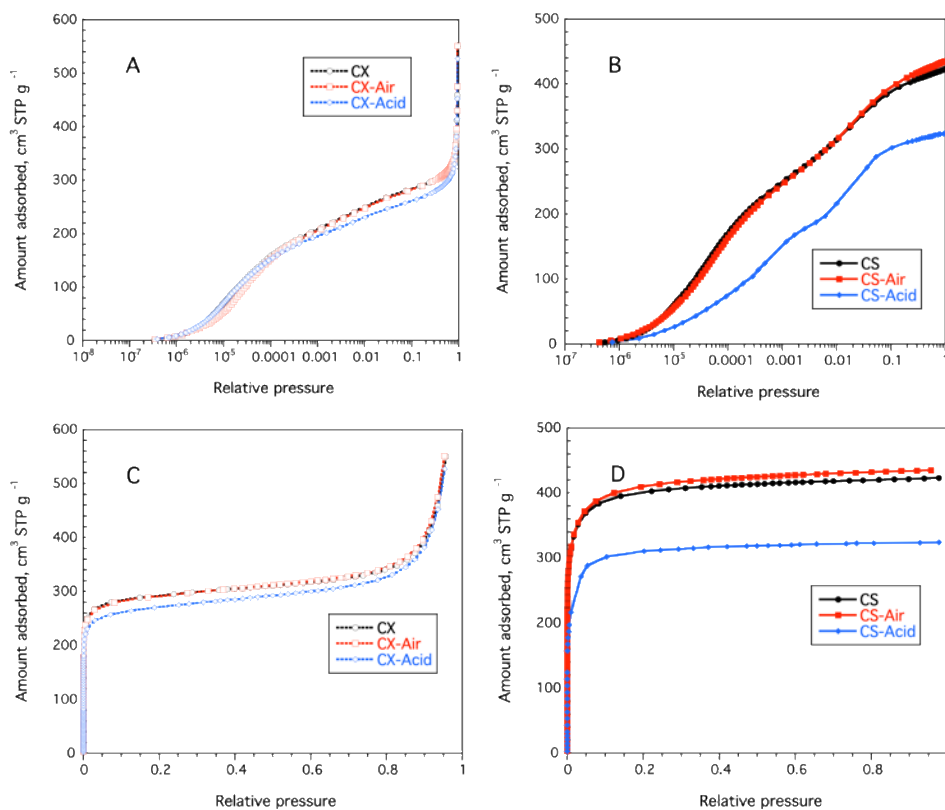Figure 5S. **Deconvolution of the C1 s and O 1s core energy level spectra of the sample studied** (related to Table 3)

Figure 6S. **Oxygen adsorption isotherms** (related to Fig 1).
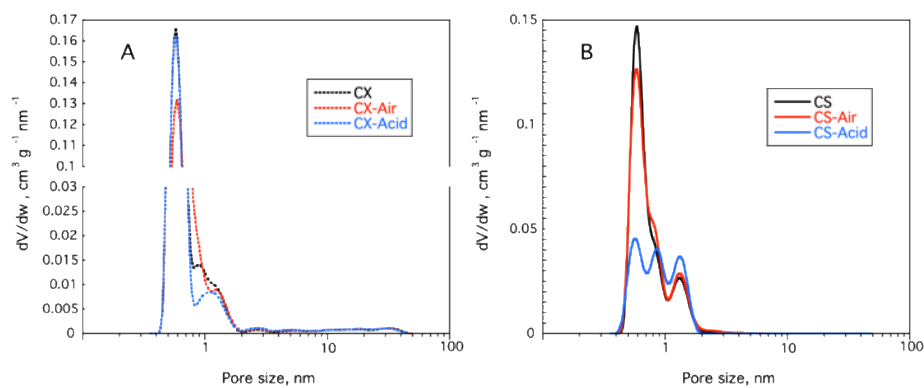(A, B) in logarithmic scale
(C, D) in linear scale

Figure 7S. **Pore size distributions calculated from O₂ adsorption isotherms** (related to Fig 1).
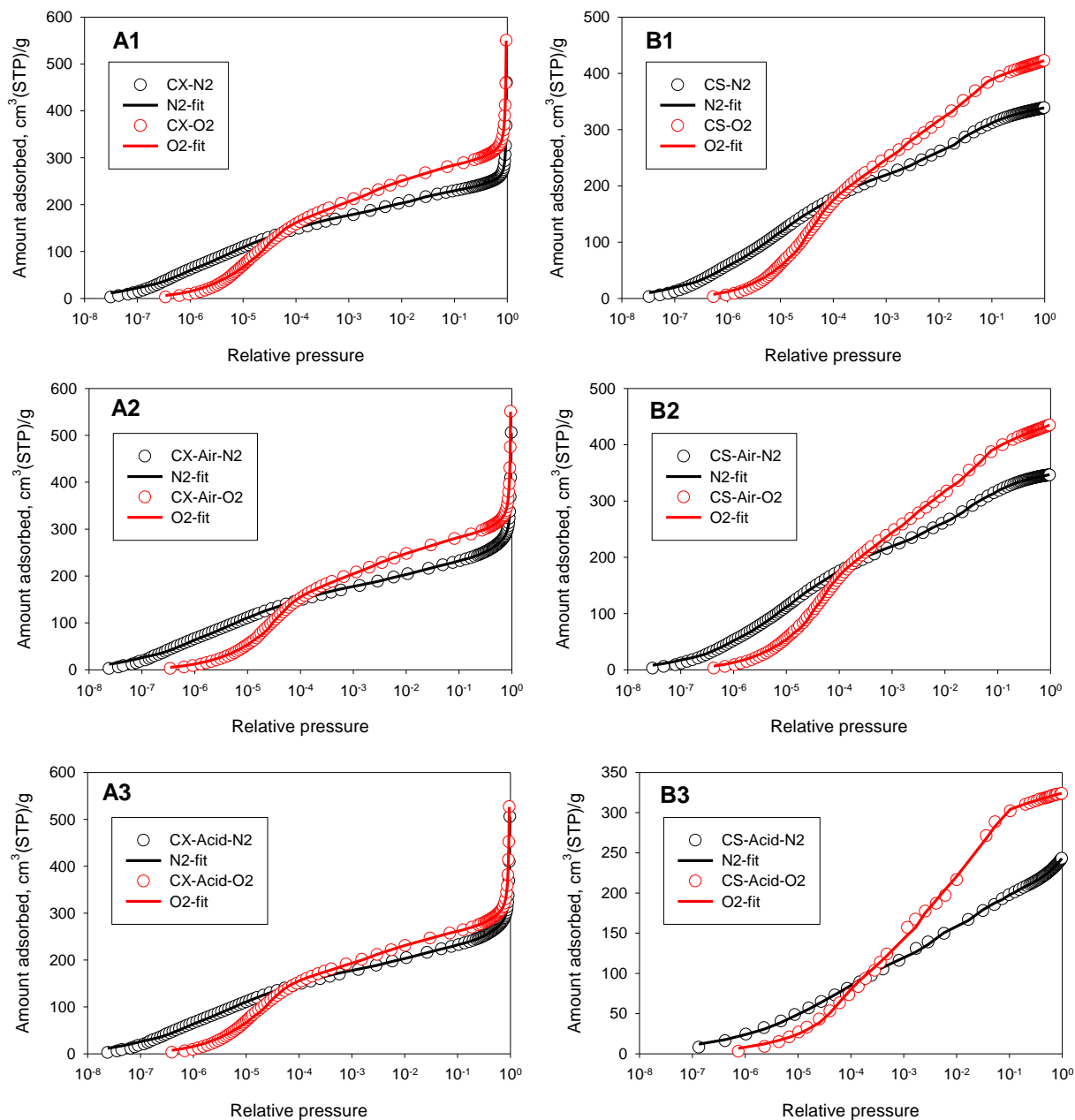
A) CX series samples
B) CS series of samples

Figure 8S. **Results of fitting the 2D-NLDFT models to experimental N₂ and O₂ isotherms measured on samples under study** (related to Fig 1).
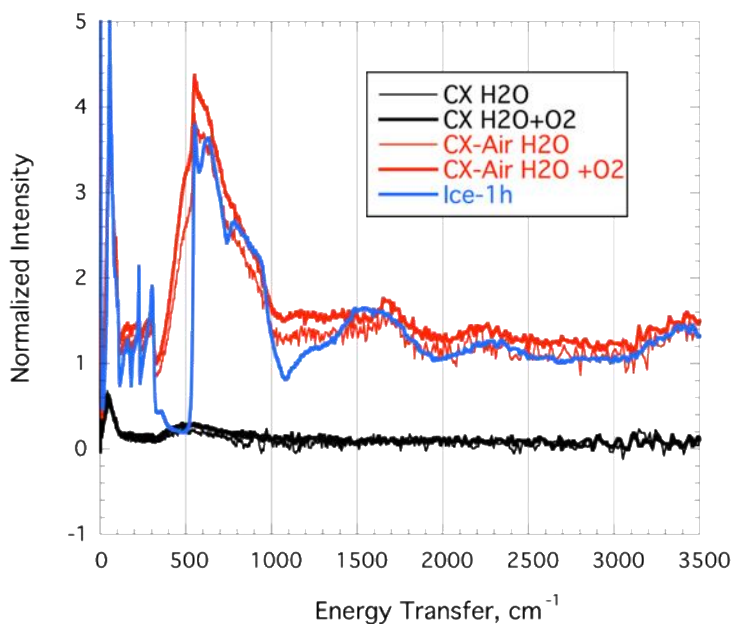
Figure 9S. **INS spectra**
CX and CX-Air spectra after exposure to water (denoted with H_2O) and exposure to water and oxygen (denoted with H_2O+O_2). The reference spectrum from ice-1h is also shown, in which two features are particularly relevant: the sharp edge between 500 and 600 cm^{-1} due to H_2O vibration, and the strong peaks below 300 cm^{-1} due to translational motions of H_2O. The minor features around 1000 cm^{-1} in the CX H_2O spectrum is due to a mis-subtraction of the C-H bending peaks when removing the signal from the blank CX sample (related to Fig 4).